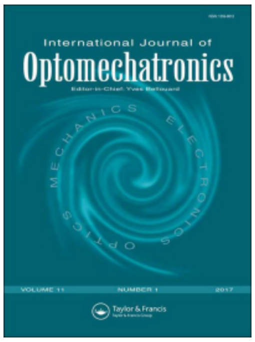

International Journal of Optomechatronics

ISSN: 1559-9612 (Print) 1559-9620 (Online) Journal homepage: www.tandfonline.com/journals/uopt20

Precision enhancement of epidural force-sensing needle with machine learning

Gichan Cho, Jongyeol Na, Myung Ho Lee, Hyun-Jung Kwon & Cheol Song

To cite this article: Gichan Cho, Jongyeol Na, Myung Ho Lee, Hyun-Jung Kwon & Cheol Song (2026) Precision enhancement of epidural force-sensing needle with machine learning, International Journal of Optomechatronics, 20:1, 2620194, DOI: 10.1080/15599612.2026.2620194

To link to this article: https://doi.org/10.1080/15599612.2026.2620194

Published online: 01 Feb 2026.

INTERNATIONAL JOURNAL OF OPTOMECHATRONICS
2026, VOL. 20, NO. 1, 2620194
https://doi.org/10.1080/15599612.2026.2620194

Precision enhancement of epidural force-sensing needle with machine learning

Gichan Cho[a], Jongyeol Na[b], Myung Ho Lee[a], Hyun-Jung Kwon[c] and Cheol Song[a,b]

[a]Department of Robotics and Mechatronics Engineering, DGIST, Daegu, Republic of Korea; [b]The Interdisciplinary Studies of Artificial Intelligence, DGIST, Daegu, Republic of Korea; [c]Department of Anesthesiology and Pain Medicine, Seoul Asan Medical Center, Seoul, Republic of Korea

ABSTRACT
Epidural injection is used in pain intervention, requiring precise needle placement within the epidural space. Traditional techniques, such as loss of resistance and fluoroscopy-guided procedures, have limitations, including reliance on subjective assessment and radiation exposure. We proposed an optical force-sensing probe with an offset criterion of the needle tip-distal end to enhance the precision of puncture detection. The offset between the needle tip and the force-sensing probe is adjusted using a piezoelectric motor-based system with feedback position control. A Long Short-Term Memory model is also trained to detect the puncture. Insertion test on silicone phantom and *ex-vivo* specimens demonstrates that the system's offset range for enhancing precision of puncture detection is between 0.6 mm and 1 mm. Compared to the offset in the previous study, the AUC score of puncture detection increased from 0.61 to 0.86. This approach secures the improvement of puncture detection reliability in robot-assisted epidural injection.

KEYWORDS
Epidural injection; Fabry-Pérot interferometer; force-sensing probe; machine learning; puncture detection

1. Introduction

An epidural injection is a widely used interventional procedure for pain management in individuals with chronic pain or pregnant women. This procedure involves inserting a needle into the spinal canal, where the spinal nerves are located, to deliver anesthetic or therapeutic drugs. Regardless of the specific technique, spinal pain interventions always require reaching the epidural space using a Tuohy epidural needle. This needle passes through the ligamentum flavum just before entering the epidural space and then stops at the designated target. In interventional procedures, identifying tissue puncture is essential for estimating the appropriate needle insertion depth. Conventional methods for detecting puncture include the loss of resistance (LOR) technique and fluoroscopy-guided procedures using a C-arm. Carm imaging provides relatively precise visualization of the needle's location within the body.[1–5] However, it also exposes practitioners to radiation risks. Various protective strategies, such as radiation shielding garments, protective barriers, and low-dose C-arm technology, help minimize exposure.[6,7] Nonetheless, due to frequent and prolonged use of fluoroscopy, physicians remain susceptible to radiation-related risks.[8,9]

Several studies have focused on developing advanced surgical tools and techniques to address the challenges faced by interventionalists.[10–18] In particular, sensing technologies have been proposed as alternatives to conventional needle guidance, allowing for precise needle positioning and puncture detection during interventions.[19] The fundamental principle behind research on detecting target tissue layer puncture is utilizing the interaction between the needle and biological tissue, drawing from the traditional loss of resistance (LOR) technique. Studies on needle-tissue interaction have revealed that a puncture event leads to a noticeable change in the force curve. Like the LOR technique, this event is characterized by a sudden drop in contact force between the needle and tissue, resulting in a distinctive

CONTACT Cheol Song csong@dgist.ac.kr Department of Robotics and Mechatronics Engineering, DGIST, Daegu, Republic of Korea.

Nomenclature

FPI	Fabry-Pérot interferometers	OPL	optical path length
OCT	optical coherence tomography	FFT	fast Fourier transform
LSTM	long short-term memory	LOR	loss of resistance
PZT	piezoelectric		

force pattern. As representative methods, probe and needle systems for spine structure identification and puncture detection have been proposed by introducing new pressure-guided devices[20] or measuring electrical bio-impedance.[21,22] These approaches have improved precision in analyzing the pressure or force applied to the needle and improve procedural safety by enabling robotic surgical systems to regulate contact force effectively. Despite the advancement of these new sensing technologies, increasing the success rate of predicting puncture events via data-driven methods remains challenging due to the variability of complex tissue structure, properties, and the dependency of sensor performance on them. To address this, researchers have turned to machine learning-based methods. Neural networks, in particular, offer the advantage of adaptively tuning parameters and recognizing puncture event patterns from force data, making them a valuable tool for increasing accuracy and safety in interventional procedures.[23]

Interferometry and laser beam sensors were often utilized to assess the critical information of a sample.[24–27] For example, the sensors offer high-resolution measurements comparable to highly sensitive force/torque sensors while maintaining a compact structure, making them well-suited for microneedle and robotic system applications.[28–37] In particular, optical sensors offer superior resolution compared to previously proposed pressure guidance systems. Furthermore, while bio-impedance sensors are vulnerable to variations in measurement performance due to their high dependence on moisture levels, optical sensors demonstrate consistent measurement performance regardless of these conditions. Among the widely used fiber-optic sensing technologies, Fiber Bragg Gratings (FBGs)[38–42] and Fabry-Pérot interferometers (FPI)[43–47] are particularly effective for force-sensing purposes. In our previous study,[48] we developed an epidural needle integrated with an FPI-based sensor to measure contact force at the needle tip. Here, we conducted a user study with interventionalists to evaluate its performance. The findings demonstrated that the system accurately tracked the force curve during the puncture process, allowing the needle to stop within the safety margins set by physicians. Despite this work, to date, there are no needle injection systems deploying optimized fiber-optic FPI-based sensor. In,[48] distinguishing the puncture event from the recorded force curve proved difficult or, in some cases, impossible, leading to a lower task success rate. Among the 10 trials for each of the 23 participants, 4 cases showed a success rate of less than 60%, when the needle design was not optimized. The previously implemented force-sensing needle provides direct contact force measurement at the needle tip. However, because the highly sensitive interferometry-based sensors is positioned at the tip, its readings are affected by both the sensor's optical properties and the Tuohy needle's curved structure. It has indicated that the force curve's shape and quality can influence the determination of the puncture event timing and the needle insertion depth.

The contribution of this work is to improve the accuracy of puncture event prediction in robotic epidural injections using configuration optimization and Long Short-Term Memory (LSTM) model training in a fiber-optic force-sensing needle. Building upon prior work on the sensor-integrated needle system,[48] we selected the offset between the needle tip and the optical force sensor as the key parameter. This offset was dynamically modified using a piezoelectric motor (PZT)-based system with simple feedback control. For each offset, we tracked the contact force and needle depth throughout the insertion process, pinpointing the exact moment of puncture. Additionally, we trained a LSTM model with timeseries data of force measurements and puncture label data. This model analyzed force curve sequences to estimate the puncture timing. Moreover, we developed a needle end-effector driven by a commercial PZT with 1 nm positional accuracy. The end-effector integrated with a commercially available 6-degree-of-freedom robotic manipulator. To evaluate its effectiveness, we experimentally demonstrate it using custom phantoms and *ex-vivo* specimens, measuring the optimized force curve and validating the system's puncture detection capabilities.

2. Materials and methods

2.1. Optical force sensing probe

To enhance the reliability of the needle-tissue interaction model measured by the system, the proposed sensor is positioned at the needle tip to measure the contact force with the tissue directly. Therefore, the sensor module must be designed to be insertable inside the needle and removable after needle positioning to allow for drug injection.

Figure 1(a) represents our interferometric system utilizing a wavelength-swept laser (Swept Laser OEM engine, AXSUN). The laser has a center wavelength of 1060 nm and a bandwidth of 100 nm. The wavelength sweeping operation rate is 100 kHz and provides a trigger signal for optical signal sampling. The signal collected through the photodetector undergoes a fast Fourier transform (FFT), followed by phase analysis of the complex optical coherence tomography (OCT) signal. Figure 1(b) shows structure and design of force-sensing probe and its working principle. We implemented a fiber-optic force sensor based on the Fabry-Pérot interferometer (FPI). The contact force sensor consists of a single-mode fiber and a reflector arranged in series, with the gap between these two optical components referred to as the Fabry-Pérot cavity (FP cavity). Previous studies on FPI have reported that the size of the FP cavity is typically formed in the range of approximately 20–25 µm. When the sensor comes into contact with a sample or biological tissue and experiences force, the distance of the FP cavity decreases. The FPI is an interferometer capable of detecting nanometric changes in the distance between the optical fiber and the reflector. Due to the optical path length (OPL) difference between the reference light reflected at the distal end of the optical fiber and the reflection light from the reflector, interference occurs between the two electromagnetic waves. Since changes in the FP cavity directly correspond to changes in the OPL, comparing the optical interference signals before and after force application allows for the quantitative measurement of the applied contact force. Also, to protect the sensor and function similarly to the stylet of a commercial epidural needle, it was enclosed in a hypodermic tube to form a probe.

The proposed contact force-sensing probe was applied to a 22 G commercial epidural needle (inner diameter: 410 µm, outer diameter: 710 µm, length: 80 mm). In pain intervention procedures, epidural needles of various sizes, ranging from 18 G to 25 G, are used depending on the patient's body type and the purpose of the procedure. In particular, 22 G or 23 G needles are commonly used for simple blocks. Accordingly, the sensing probe was designed and applied specifically for a 22 G epidural needle in this study. This allows the contact force to be estimated in real time based on the phase value of the interference signal. Additionally, it was mechanically coupled using a bolt in a custom stylet hub to fix the sensing probe in an optimized position securely. This design enables offset adjustment between the probe and the needle tip. As an adjustable parameter for optimizing the contact force-sensing epidural needle

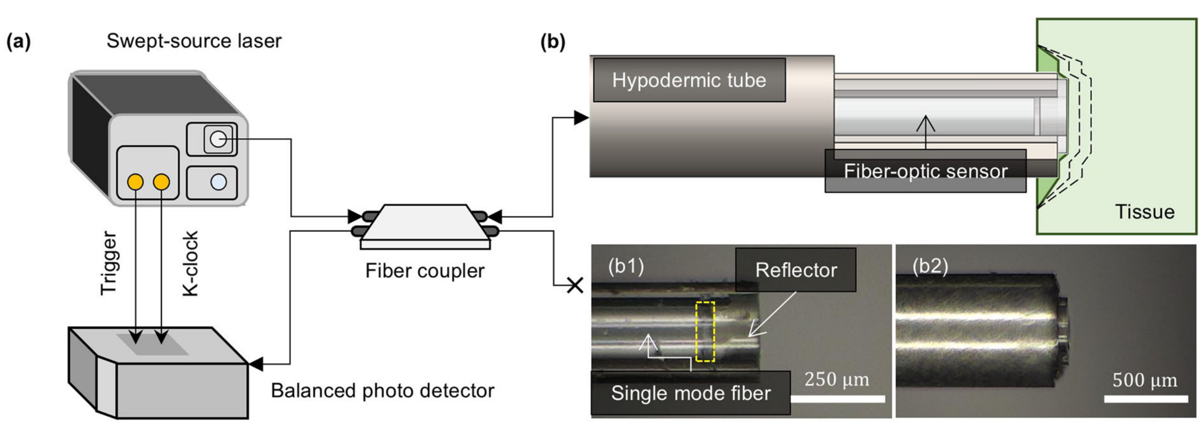

Figure 1. Optical system configuration and implemented force-sensing probe. (a) Common-path optical coherence tomography with swept-source tunable laser. (b) Contact force-sensing probe. (b1) Implemented Fabry-Pérot interferometer with air cavity(yellow dashed box). (b2) A fiber-optic sensor encapsulated in a hypodermic tube.

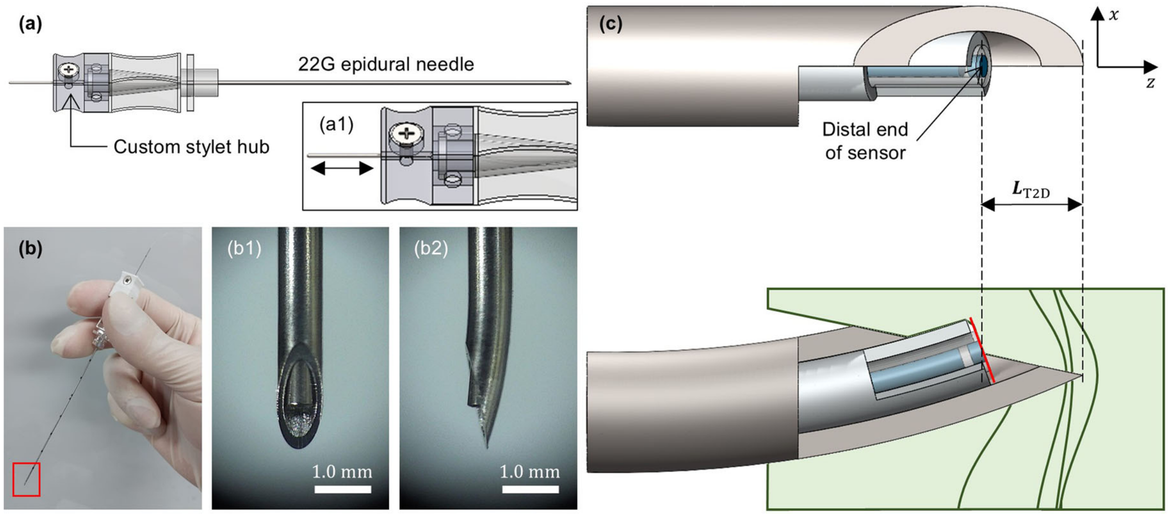

Figure 2. Integrated force-sensing epidural needle. (a) Integration of the optical sensor using a custom stylet hub. (b) Configuration of optical sensor embedded epidural needle. (b1) *xz*-Plane view. (b2) *yz*-Plane view. (c) Force sensing mechanism in soft tissue, and principal optimization parameter.

configuration, we selected the offset between the needle tip (T) and the distal end of the probe (D). Figure 2(c) illustrates the scenario when the proposed system penetrates a multi-layer tissue. As the needle tip advances, it cuts through the anterior tissue and progresses in the depth direction, causing

Some tissue to be pushed into the needle. At this point, the probe measures the contact force exerted by the displaced tissue inside the needle. Due to this measurement mechanism, the needle tip-to-distal end L_{T2D} offset can influence the measured puncture force's magnitude, the force curve's shape, and the needle depth at which the puncture is detected. These factors must be carefully considered to establish optimal conditions for puncture detection.

2.2. Sensor calibration

Sensor calibration was performed to confirm the linear proportionality between the contact force caused by the interaction between the soft tissue and the system and the phase measured by the sensor, and identify the parameters between the two variables.

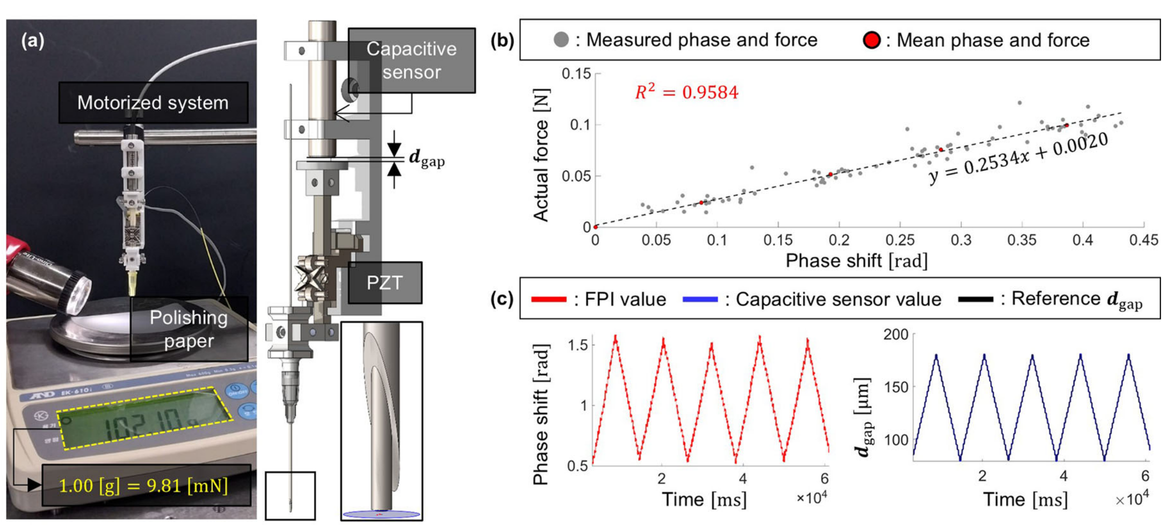

Figure 3. Calibration of the injection system. (a) Balance-based contact force-phase calibration setup. (b) Linear relationship between contact force and phase shift. (c) Repeatability test of implemented sensor.

As shown in Figure 3(a), we used an experimental setup to measure the contact force applied to the forcesensing probe and the corresponding FPI phase shift. The setup consists of a motorized system based on a piezoelectric (PZT) motor and a precision balance. A precision balance (measurement range of 600 g, resolution of 0.01 g, EK-610i, A&D) was used to apply a contact force to the force-sensing probe and obtain a quantitative reading in weight units. An optical polishing paper was placed between the balance's plate and probe to prevent sensor damage during calibration. The measured weight was then converted to the actual force value using the relation 1 g = 0.0098N. The PZT motor-based motorized system (positional resolution of 1 nm, LEGS-LL1011A, PiezoMotor) moves the force-sensing probe to stably load or unload a contact force onto the balance at a constant velocity. A 5 g pre-load was first established on the balance. Subsequently, the motorized system applied an additional positive force of 15 g (approximately 0.15 N) in 3 g increments, up to a total force of 20 g. Figure 3(b) shows the calculated correlation parameters between the force variation (Δ_F) and the phase shift (Δ_ϕ), based on data from 20 repeated measurements under same process and condition. Also the R-squared value of phase-force regression model was 0.9584. Finally, as shown in Figure 3(c), the repeatability of the contact force measurement was tested by inducing a repetitive sawtooth motion with the PZT motor. A capacitive sensor (measurement range of 500 μm, resolution of 3 nm, C8-3.2, Lion Precision, USA) measured the real-time position of the PZT motor. Cyclic loading and unloading of the contact force applied to the probe resulted in a phase shift with a sawtooth waveform, closely mirroring the trend observed in the gap sensor. This result confirms the linearity and repeatability of the proposed optical force-sensing probe.

2.3. Tip-distal end offset regulation

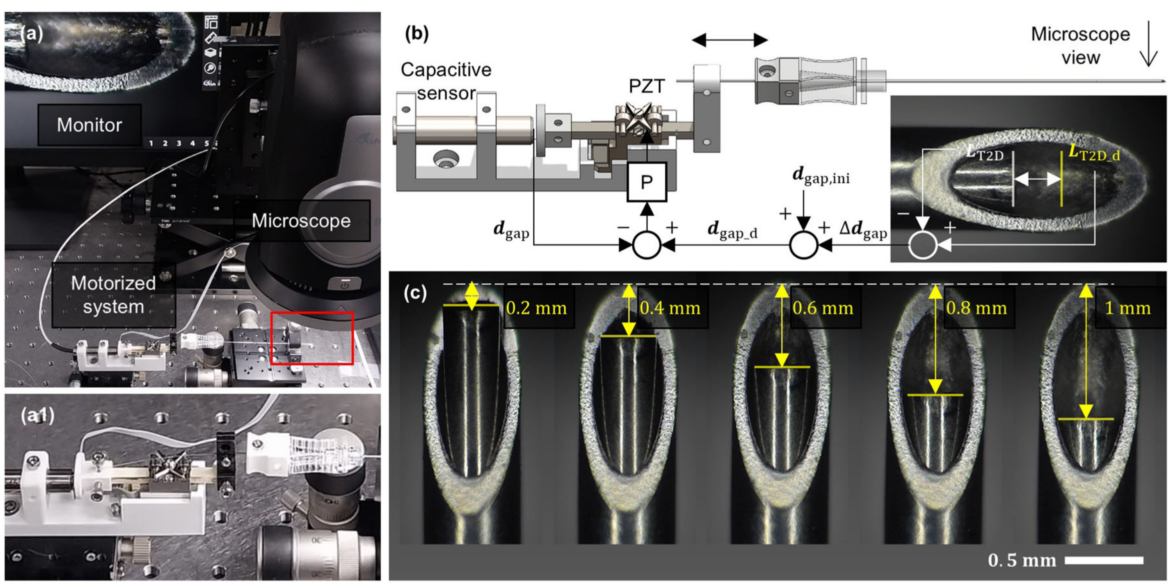

Figure 4. Needle tip to distal end offset adjustment. (a) Experimental setup for tip-distal end offset regulation. (b) Microscope-guided adjustment of the tip-distal end offset using PZT motor position control. (c) Offset adjustment results.

As depicted in Figure 4(a), we prepared a microscope-guided setup to more precisely regulate the distance between the needle tip and the probe's distal end, which can affect the phase shift-based contact force measurement. This setup also utilized the motorized system composed of the PZT motor and a capacitive sensor. We determined the offset between the needle tip and the distal end of the force-sensing probe, denoted as L_{T2D}, using a microscopic view. As shown in Figure 4(b), the offset between the needle tip and the probe was adjusted by moving the linear PZT motor to compensate for the error, Δd_{gap}, between the desired offset (L_{T2Dd}) and the measured offset (L_{T2D}). To control the PZT motor, we employed a proportional control scheme that generates a motor output proportional to the error between the desired motor position (d_{gapd}) and the current motor position (d_{gap}) measured by a capacitive sensor. Based on the epidural needle model used in this study, the probe was visually identifiable within a range of up to 1 mm from the needle tip. Therefore, the L_{T2D} offset was adjusted from 0 mm to 1 mm in 0.2 mm increments, and the force curve and puncture detection were analyzed for each case. Each offset was regulated with a precision of ±0.02 mm.

2.4. Long Short-Term Memory for puncture detection

Unlike simple needle-tissue interaction scenarios, the puncture event is mathematically challenging to describe. Particularly in epidural injection applications, the mechanical properties of the ligamentum flavum vary significantly due to factors such as the patient's age, gender, and spinal disorders. Various collaborative robot and robot-assisted surgery studies have utilized artificial intelligence models to address these unpredictable situations. Long Short-Term Memory (LSTM) is a model frequently used for time-series data prediction. Therefore, it is applied in various applications, such as predicting external torque acting on robots, detecting collisions,[49] and estimating the motion or interaction force of microsurgical robot end-effectors.[50–53] We trained an LSTM model using the puncture task data obtained from the developed contact force-sensing needle with different needle configurations. We used a silicone phantom to acquire the puncture data required for model training, as shown in Figure 5(a). The LSTM model was trained using inputs of the phase shift (proportional to the contact force) and a corresponding smooth label associated with the puncture timing of the silicone phantom. The phantom was a silicone pad with an elastic modulus of approximately 0.75 N/mm^2 and a thickness of 3.5 mm. Previous research on the mechanical properties of the ligamentum flavum in the lumbar spine indicates that Young's modulus in humans ranges from about 2.4 MPa to 4.6 MPa,[54] with a thickness of 2.5 mm to 4.5 mm on average.[55] Although the silicone phantom is softer, it provides sufficient stiffness to detect the puncture event. A PZT motor was used to drive the needle with a constant open-loop input. Similar to the loss of resistance technique, force sensing was continuously performed as the needle was inserted. The open-loop control scheme was selected to halt the motion when the puncture event was manually detected. The PZT motor had a scaling factor ($\hat{m}$) of approximately 11.5 µm/s, measured in both positive and negative directions for output speed relative to the control input. During the puncture

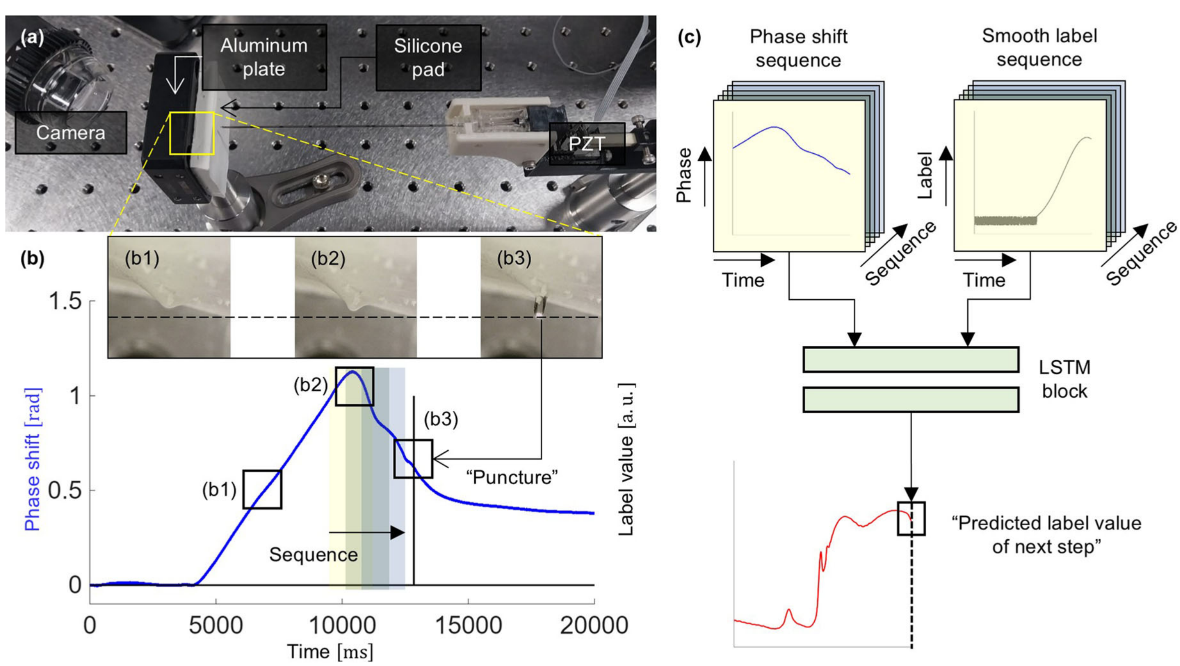

Figure 5. Data acquisition process for LSTM-based puncture detection. (a) Silicone phantom-based experimental setup. (b) Criteria for puncture event annotation. (b1) Rising stage. (b2) Maximum contact force stage. (b3) Puncture of silicone pad layer. (c) LSTM model architecture for puncture detection using phase (contact force) and smooth label.

procedure, we recorded the contact force measured by the force-sensing probe and a corresponding hard label to denote the moment of puncture. By observing the camera view, the complete puncture event was defined as the instant the needle tip was visually confirmed to have pierced the silicone pad (Figure 5(b3)). However, using a hard label directly can lead to inaccuracies in model training and increase the risk of overfitting. As depicted in Figure 5(c), a label smoothing technique was applied to generate a refined label to mitigate this issue. The architecture of the LSTM model for puncture detection consists of two layers and a hidden size of 512. The LSTM model was trained to ultimately output the probability of tissue puncture (true or false) as a value between 0 and 1, based on the input phase values. Therefore, we utilized binary cross-entropy, which is considered more suitable for such binary classification problems, as the loss function. A learning rate of 1e−5 and the Adam optimizer were used for training.

3. Results and discussion

3.1. Puncture force curve corresponded to offset

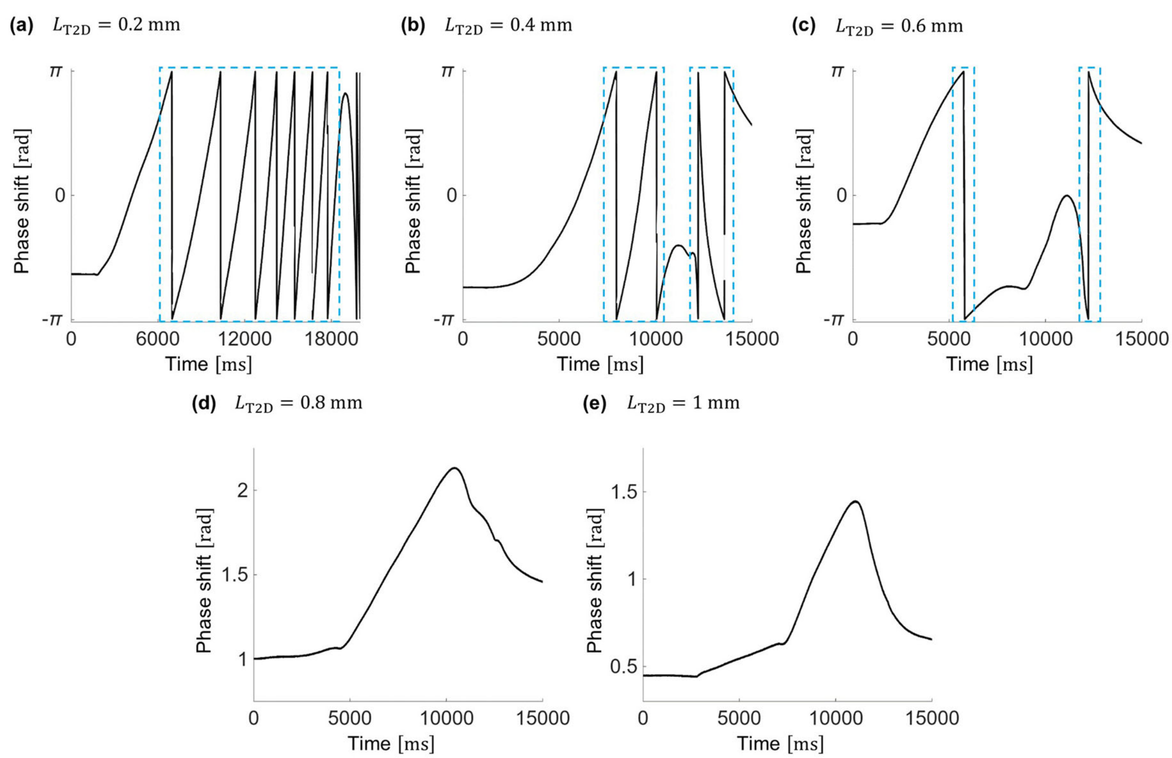

Figure 6. (a)–(e) Representative contact force curve during phantom studies of each needle tip to distal end offset (from 0.2 mm to 1 mm) cases for force-sensing needle. The raw phase data is wrapped between $+\pi$ and $-\pi$ (sky blue dashed box).

Figure 6 illustrates the force curves recorded during the puncture of a phantom using force-sensing needles with different configurations. Analysis of the measured contact force curves revealed that in configurations with an $_{LT2D}$ of 0.6 mm or greater, the maximum phase shifts recorded prior to puncture were 5.12 ± 1.05 rad, 1.21 ± 0.14 rad, 0.97 ± 0.05 rad, respectively. Conversely, in the 0.2 mm and 0.4 mm configurations, the contact force increased to 45.47 ± 2.24 rad, 11.65 ± 1.08 rad, respectively. Specifically, at offsets between 0.2 mm and 0.4 mm (Figure 6(a), (b)), this significant rise in force caused the raw phase data to exhibit multiple wrapping points. Furthermore, at the 0.2 mm offset, where the needle tip is nearly flush with the probe, the needle failed to cut the anterior tissue layers smoothly, impeding the needle puncture task. Therefore, considering the ease of signal processing for the machine learningbased puncture detection algorithm and safety in a practical clinical scenario, the conclusion from the phantom tests was that the proposed force-sensing needle should be configured with a tip-distal end offset between 0.6 mm and 1 mm.

3.2. Machine learning-based puncture detection

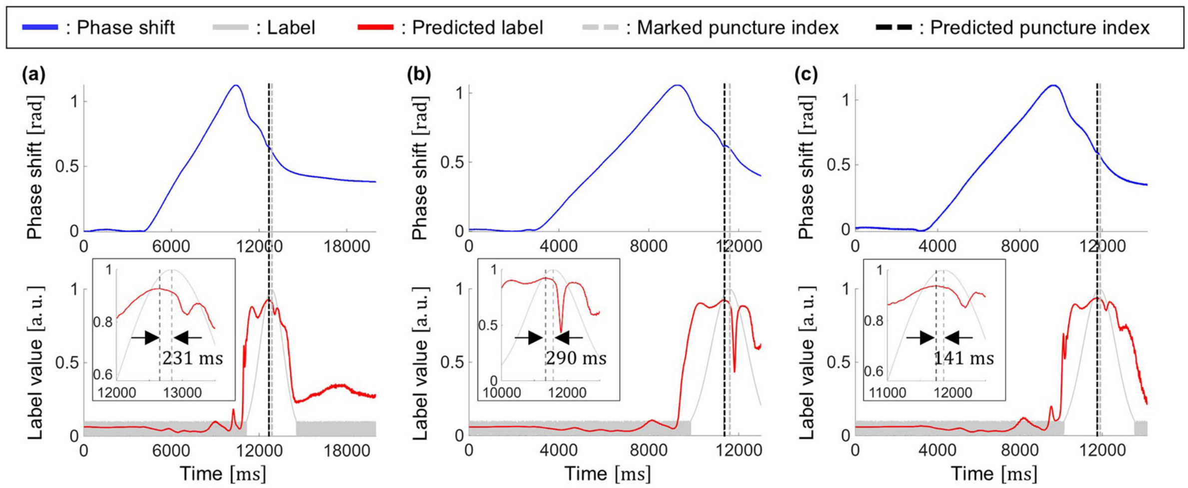

Figure 7. (a)–(c) Representative puncture event prediction results using LSTM algorithm.

The LSTM model was trained using the input of the contact force and puncture index label. In the previous section, we acquired 22 datasets per case by conducting 22 penetration experiments for each needle tip-distal end offset. We split the data into training and validation sets with an 86:14 ratio; consequently, for each case, 19 datasets were utilized to train the LSTM model, and three datasets were used for validation.

As illustrated in Figure 7(a)–(c), the trained model predicts the probability of a puncture event occurring based on the force curve, with output values ranging from 0 to 1. When tested using unwrapped data within 0.6 mm and 1 mm offset range, the trained LSTM model achieved an AUC score of 0.86. On the other hand, when the test was conducted using force curve data from a force-sensing needle configured with a much smaller offset, the prediction accuracy decreased significantly due to multiple phase wrapping points. Notably, the configuration with a 0.5 mm offset, which was used in a previous study,[47] only achieved an AUC score of 0.61. This result implies that the offset criteria identified in our study are essential for achieving significantly better performance in AI model-based puncture prediction.

Furthermore, in representative test results, the LSTM model predicted the puncture event to occur between 141 ms and 290 ms earlier than the experimentally recorded puncture label. Considering the velocity of the PZT motor, this slight time difference does not correspond to a meaningful change in the needle's penetration depth into the target region. However, from a clinical safety perspective, the model's ability to predict the puncture slightly ahead of the actual event is noteworthy.

3.3. Ex-vivo experimental validation

The $_{ex\text{-}vivo}$ experiments utilized a porcine spine as the target specimen. Testing was conducted with a fixed offset of 0.7 mm between the needle tip and the probe, chosen as the midpoint of the optimal force-sensing needle design criteria. The experimental setup is illustrated in Figure 8. The needle actuation mechanism was integrated into an injection end-effector powered by a piezoelectric motor (PZT), which enables precise motion despite its limited stroke. As depicted in Figure 8(b1) and (b2), the initial needle insertion was performed slightly off-center from the spine to prevent direct contact with the bone. Before initiating the puncture process, the needle was inserted approximately 3 cm. Additionally, a 6-DoF robot manipulator was used to compensate for the PZT's short stroke and assist with the prepositioning of the needle. Across 10 test trials, the average needle penetration depth at the moment of puncture detection was recorded at 1.3 mm.

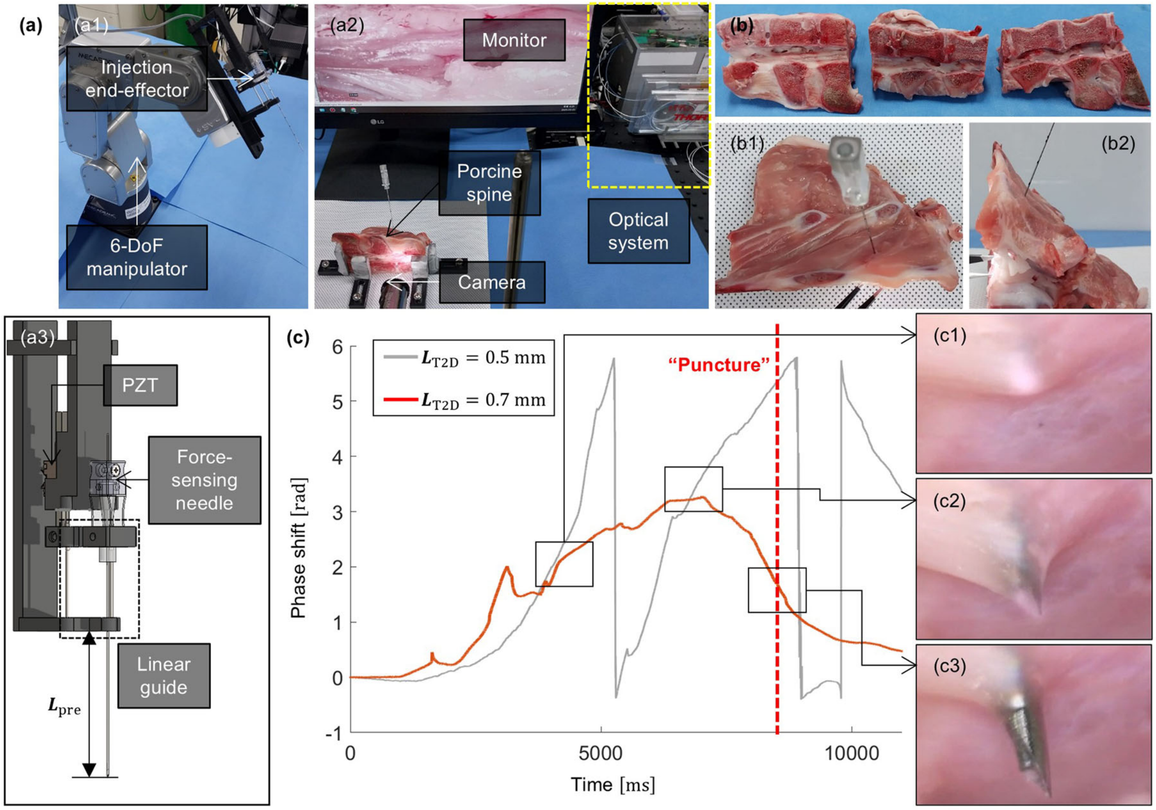

Figure 8. The insertion test results on porcine spine. (a) Experimental setup. (a1) Robotic system with 6-DoF manipulator, and injection end-effector. (a2) Optical system and porcine spine. (a3) Injection end-effector. (b) Porcine spine. (b1) Needle insertion position in the anterior-posterior (AP) view. (b2) Needle insertion angle in inferior view. (c) Phase shift proportion to the contact force during needle insertion. (c1) Rising stage. (c2) Maximum contact force stage. (c3) Puncture of ligamentum flavum.

4. Conclusion

This study presents an optimal contact force sensing system configuration to enhance puncture detection accuracy in robotic epidural injection procedures. Detecting puncture events in target tissue layers ensures precision and safety in robot-assisted surgical systems. We developed an optical force-sensing probe integrated into an epidural needle to improve the reliability of force measurements during needletissue interactions. Additionally, we designed a high-precision robotic end-effector driven by a motorized system. By analyzing penetration test data from various sensing system configurations—each with different offsets between the needle tip and distal end, we trained an LSTM model for puncture detection. The results strongly correlate with system design optimization and puncture detection performance. This study advances robotic-assisted interventions, providing a safer and more accurate alternative for needle-based medical procedures. Future work will focus on developing control algorithms for an optimally designed robotic epidural injection system aligned with procedural workflows. Furthermore, the proposed sensor and robotic system and the optimization process have the potential for broader applications in medical procedures requiring high-precision force measurements, such as brain and laparoscopic surgeries.

Disclosure statement

No potential conflicts of interest were reported by the author(s).

Funding

This work was supported by the Technology Innovation Program [20023168, Development of clinician collaborative robot platform technology for 3 types of pain interventional procedures based on crossdrug handler and instrument modules] funded by the Ministry of Trade, Industry & Energy (MOTIE, Korea).

References

[1] Kim, D. H.; Kwon, H. J.; Jeon, B.; Lee, D.; Shin, J. W.; Choi, S. S. Comparison of the Contralateral Oblique View with the Lateral View for Mid-Thoracic Epidural Access Under Fluoroscopic Guidance: A Randomized Controlled Trial. *Reg. Anesth. Pain Med.* **2022**, *47*, 453–458. DOI: 10.1136/rapm-2021-103466.

[2] Wagner, A. L. Ct Fluoroscopy–Guided Epidural Injections: Technique and Results. *Am. J. Neuroradiol.* **2004**, *25*, 1821–1823.

[3] Plastaras, C. T.; Popescu, A.; McLaughlin, C. A.; Sanderson, S. O.; Biaesch, A. G.; Bosley, J. C.; Kaplan, B.; Pukenas, B. A. C-Arm Fluoroscope Angle Settings for Fluoroscopically Guided Lumbar Transforaminal Epidural Injections. *Pain Med.* **2016**, *17*, 832–838. DOI: 10.1093/pm/pnv013.

[4] Tamjid Ali, M.; Khasru, M. R.; Salek, A.; Sikdar, A.; Haque, Q. T. Outcome of c-Arm Guided Epidural Steroid Injections in Patients with Prolapsed Lumbar Intervertebral Disc with Radiculopathy. *J. Orthop. Sports Med.* **2023**, *5*, 286–292.

[5] Gao, C.; Phalen, H.; Margalit, A.; Ma, J. H.; Ku, P. C.; Unberath, M.; Taylor, R. H.; Jain, A.; Armand, M. Fluoroscopy-Guided Robotic System for Transforaminal Lumbar Epidural Injections. *IEEE Trans. Med. Robot. Bionics.* **2022**, *4*, 901–909. DOI: 10.1109/tmrb.2022.3196321.

[6] Choi, E. J.; Go, G.; Han, W. K.; Lee, P. B. Radiation Exposure to the Eyes and Thyroid during c-Arm Fluoroscopy-Guided Cervical Epidural Injections is Far below the Safety Limit. *Kor. J. Pain.* **2020**, *33*, 73–80. DOI: 10.3344/kjp.2020.33.1.73.

[7] Zhitny, V. P.; Do, K.; Kawana, E.; Do, J.; Wajda, M. C.; Gualtier, R. T.; Goodman, A. J.; Zou, S. Radiation Exposure in Interventional Pain Management Physicians: A Systematic Review of the Current Literature. *Pain Physician.* **2024**, *27*, E17–E35. DOI: 10.36076/ppj.2024.27.E17.

[8] Shim, D. M.; Kim, Y. M.; Oh, S. K.; Lim, C. M.; Kown, B. T. Radiation Induced Hand Necrosis of an Orthopaedic Surgeon Who Had Treated a Patient with Fluoroscopy-Guided Spine Injection. *J. Kor. Orthop. Assoc.* **2014**, *49*, 250–254. DOI: 10.4055/jkoa.2014.49.3.250.

[9] Jacob, S.; Boveda, S.; Bar, O.; Brézin, A.; Maccia, C.; Laurier, D.; Bernier, M. O. Interventional Cardiologists and Risk of Radiation-Induced Cataract: results of a French Multicenter Observational Study. *Int. J. Cardiol.* **2013**, *167*, 1843–1847. DOI: 10.1016/j.ijcard.2012.04.124.

[10] Simone, C.; Okamura, A. M. 2002 Modeling of Needle Insertion Forces for Robot-Assisted Percutaneous Therapy. In *Proceedings. 2002 IEEE International Conference on Robotics and Automation (Cat. No. 02CH37292)*, Vol. *2*. IEEE, Washington, D.C., United States, pp. 2085–2091. DOI: 10.1109/ROBOT.2002.1014848.

[11] Crouch, J. R.; Schneider, C. M.; Wainer, J.; Okamura, A. M. A Velocity-Dependent Model for Needle Insertion in Soft Tissue. In *International Conference on Medical Image Computing and Computer-Assisted Intervention,* California, United States, 2005, 624–632.

[12] Zhai, J.; Karuppasamy, K.; Zvavanjanja, R.; Fisher, M.; Fisher, A.; Gould, D.; How, T. A Sensor for Needle Puncture Force Measurement During Interventional Radiological Procedures. *Med. Eng. Phys.* **2013**, *35*, 350–356. DOI: 10.1016/j.medengphy.2012.05.012.

[13] Bao, Y. d.; Qu, S. q.; Qi, D. b.; Wei, W. Investigation on Puncture Mechanical Performance of Tracheal Tissue. *J. Mech. Behav. Biomed. Mater.* **2022**, *125*, 104958. DOI: 10.1016/j.jmbbm.2021.104958.

[14] Barbé, L.; Bayle, B.; de Mathelin, M.; Gangi, A. In Vivo Model Estimation and Haptic Characterization of Needle Insertions. *Int. J. Rob. Res.* **2007**, *26*, 1283–1301.

[15] Pappalardo, A.; Albakri, A.; Liu, C.; Bascetta, L.; De Momi, E.; Poignet, P. Hunt–Crossley Model Based Force Control for Minimally Invasive Robotic Surgery. *Biomed. Signal Process. Control* **2016**, *29*, 31–43. DOI: 10.1016/j.bspc.2016.05.003.

[16] Liang, W.; Ma, J.; Tan, K. K. Contact Force Control on Soft Membrane for an Ear Surgical Device. *IEEE Trans. Ind. Electron.* **2018**, *65*, 9593–9603. DOI: 10.1109/TIE.2018.2818647.

[17] Misra, S.; Reed, K. B.; Schafer, B. W.; Ramesh, K.; Okamura, A. M. Mechanics of Flexible Needles Robotically Steered Through Soft Tissue. *Int. J. Rob. Res.* **2010**, *29*, 1640–1660. DOI: 10.1177/0278364910369714.

[18] Okamura, A. M.; Simone, C.; O'Leary, M. D. Force Modeling for Needle Insertion into Soft Tissue. *IEEE Trans. Biomed. Eng.* **2004**, *51*, 1707–1716. DOI: 10.1109/TBME.2004.831542.

[19] Cheng, Z.; Koskinopoulou, M.; Bano, S.; Stoyanov, D.; Savarimuthu, T. R.; Mattos, L. S. Sensing Technologies for Guidance during Needle-Based Interventions. *IEEE Trans. Instrum. Meas.* **2024**, *73*, 1–15. DOI: 10.1109/TIM.2024.3441017.

[20] Capogna, G.; Coccoluto, A.; Capogna, E.; Del Vecchio, A. Objective Evaluation of a New Epidural Simulator by the Compuflo® Epidural Instrument. *Anesthesiol. Res. Pract.* **2018**, *2018*, 4710263–4710266. DOI: 10.1155/2018/4710263.

[21] Halonen, S.; Annala, K.; Kari, J.; Jokinen, S.; Lumme, A.; Kronström, K.; Yli-Hankala, A. Detection of Spine Structures with Bioimpedance Probe (Bip) Needle in Clinical Lumbar Punctures. *J. Clin. Monit. Comput.* **2017**, *31*, 1065–1072. DOI: 10.1007/s10877-016-9915-8.

[22] Yun, J.; Kim, H. W.; Lee, J. H. Improvement of Depth Profiling into Biotissues Using Micro Electrical Impedance Spectroscopy on a Needle with Selective Passivation. *Sensors* **2016**, *16*, 2207. DOI: 10.3390/s16122207.

[23] Li, Y.; Li, H. Penetration Event Identification Based on Neural Network for Needle Tip Location in Robot Assisted Lumbar Puncture Surgery. *IEEE Robot. Autom. Lett.* **2024**, *9*, 343–350. DOI: 10.1109/LRA.2023.3333236.

[24] Song, C.; Kim, T. J.; Gweon, D. G. Beam Scanning Confocal Differential Heterodyne Interferometry. *Int. J. Optomechatronics* **2007**, *1*, 27–45. DOI: 10.1080/15599610701261076.

[25] Zhang, J.; Li, Y.; Yao, G. All Fiber Mach–Zehnder Interferometer for Simultaneous Measurement of Temperature and Refractive Index. *Int. J. Optomechatronics* **2023**, *17*, 2182389. DOI: 10.1080/15599612.2023.2182389.

[26] Ma, Y.; Liu, W.; Liu, X.; Wang, N.; Zhang, H. Review of Sensing and Actuation Technologies–from Optical Mems and Nanophotonics to Photonic Nanosystems. *Int. J. Optomechatronics* **2024**, *18*, 2342279. DOI: 10.1080/15599612.2024.2342279.

[27] Yeo, C.; Chang, Y.; Song, C. High-Speed Tissue Metabolism Measurement Using a Combination of Diffuse Speckle Contrast Analysis and near-Infrared Spectroscopy. *Int. J. Optomechatronics* **2024**, *18*, 2382141. DOI: 10.1080/15599612.2024.2382141.

[28] Giudice, G. D.; Orekhov, A. L.; Shen, J. H.; Joos, K. M.; Simaan, N. Investigation of Micromotion Kinematics of Continuum Robots for Volumetric Oct and Oct-Guided Visual Servoing. *IEEE/ASME Trans. Mechatron.* **2021**, *26*, 2604–2615. DOI: 10.1109/TMECH.2020.3043438.

[29] Song, C.; Gehlbach, P. L.; Kang, J. U. Active Tremor Cancellation by a “Smart” Handheld Vitreoretinal Microsurgical Tool Using Swept Source Optical Coherence Tomography. *Opt. Express.* **2012**, *20*, 23414–23421. DOI: 10.1364/OE.20.023414.

[30] Song, C.; Gehlbach, P. L.; Kang, J. Swept Source Optical Coherence Tomography Based Smart Handheld Vitreoretinal Microsurgical Tool for Tremor Suppression. *Annu. Int. Conf. IEEE Eng. Med. Biol. Soc.* **2012**, *2012*, 1405–1408. DOI: 10.1109/EMBC.2012.6346202.

[31] Song, C.; Park, D. Y.; Gehlbach, P. L.; Park, S. J.; Kang, J. U. Fiber-Optic Oct Sensor Guided “Smart” Micro-Forceps for Microsurgery. *Biomed. Opt. Express.* **2013**, *4*, 1045–1050. DOI: 10.1364/BOE.4.001045.

[32] Park, H. C.; Yeo, C. B.; Gehlbach, P. L.; Song, C. Development of the Dual SMART Micro-Surgical System Using Common-Path Swept Source Optical Coherence Tomography. In *2015 37th Annual International Conference of the IEEE Engineering in Medicine and Biology Society (EMBC),* Milano, Italy, 2015, 5–8. DOI: 10.1109/EMBC.2015.7318247.

[33] Koo, D.; Park, H. C.; Gehlbach, P. L.; Song, C. Development and Preliminary Results of Bimanual Smart Micro-Surgical System Using a Ball-Lens Coupled Oct Distance Sensor. *Biomed. Opt. Express.* **2016**, *7*, 4816–4826. DOI: 10.1364/BOE.7.004816.

[34] Yeo, C.; Park, H. C.; Jang, S.; Gehlbach, P. L.; Song, C. Dual Optical Coherence Tomography Sensor Guided, Two-Motor, Horizontal Smart Micro-Scissors. *Opt. Lett.* **2016**, *41*, 4723–4726. DOI: 10.1364/OL.41.004723.

[35] Im, J.; Song, C. Oblique Injection Depth Correction by a Two Parallel Oct Sensor Guided Handheld Smart Injector. *Biomed. Opt. Express.* **2021**, *12*, 926–939. DOI: 10.1364/BOE.410492.

[36] Im, J.; Park, S.; Song, C. Handheld Motorized Injection System with Fiber-Optic Distance Sensors and Adaptive Time-Delay Controller. *Int. J. Optomechatronics* **2024**, *18*, 2299023. DOI: 10.1080/15599612.2023.2299023.

[37] Wang, C.; Liu, Y.; Calle, P.; Li, X.; Liu, R.; Zhang, Q.; Yan, F.; Fung, K.; Conner, A. K.; Chen, S.; et al. Enhancing Epidural Needle Guidance Using a Polarization-Sensitive Optical Coherence Tomography Probe with Convolutional Neural Networks. *J. Biophotonics.* **2024**, *17*, e202300330. DOI: 10.1002/jbio.202300330.

[38] Beisenova, A.; Issatayeva, A.; Tosi, D.; Molardi, C. Fiber-Optic Distributed Strain Sensing Needle for Real-Time Guidance in Epidural Anesthesia. *IEEE Sensors J.* **2018**, *18*, 8034–8044. DOI: 10.1109/JSEN.2018.2865220.

[39] Carotenuto, B.; Micco, A.; Ricciardi, A.; Amorizzo, E.; Mercieri, M.; Cutolo, A.; Cusano, A. Optical Guidance Systems for Epidural Space Identification. *IEEE J. Select. Topics Quantum Electron.* **2017**, *23*, 371–379. DOI: 10.1109/JSTQE.2016.2600027.

[40] Elayaperumal, S.; Bae, J. H.; Daniel, B. L.; Cutkosky, M. R. Detection of Membrane Puncture with Haptic Feedback Using a Tip-Force Sensing Needle. In *2014 IEEE/RSJ International Conference on Intelligent Robots and Systems,* Hong Kong, China, 2014, 3975–3981. DOI: 10.1109/IROS.2014.6943121.

[41] Barz, S.; Friedemann, M.; Voigt, S.; Melloh, M.; Barz, T. Epidural Pressure Measurement Using a Fiberoptic Sensor (Proof-of-Principle in Vivo Animal Trial). *Animal Model. Exp. Med.* **2024**, *7*, 769–776. DOI: 10.1002/ame2.12469.

[42] Zhang, T.; Chen, B.; Zuo, S. A Novel 3-Dof Force Sensing Microneedle with Integrated Fiber Bragg Grating for Microsurgery. *IEEE Trans. Ind. Electron.* **2022**, *69*, 940–949. DOI: 10.1109/TIE.2021.3055173.

[43] Mo, Z.; Li, J.; Xu, W. Tactile Needle Probe for Minimally Invasive Tissue Identification during Epidural Space Insertion. *Optik. (Stuttg)* **2021**, *242*, 167285. DOI: 10.1016/j.ijleo.2021.167285.

[44] Li, R.; Zhao, X.; Ma, B.; Lin, Z.; Tan, Y. A Highly Integrated Biomedical Pressure-Temperature Sensor. *IEEE Sensors J.* **2024**, *24*, 32203–32212. DOI: 10.1109/JSEN.2024.3450672.

[45] Liu, X.; Iordachita, I. I.; He, X.; Taylor, R. H.; Kang, J. U. Miniature Fiber-Optic Force Sensor Based on Lowcoherence Fabry-Pérot Interferometry for Vitreoretinal Microsurgery. *Biomed. Opt. Express.* **2012**, *3*, 1062–1076. DOI: 10.1364/BOE.3.001062.

[46] Uzun, D.; Ulgen, O.; Kocaturk, O. Optical Force Sensor with Enhanced Resolution for Mri Guided Biopsy. *IEEE Sensors J.* **2020**, *20*, 9202–9208. DOI: 10.1109/JSEN.2020.2988816.

[47] Im, J.; Cho, G.; Song, C. Compact Fiber-Optic Sensor for Simultaneous Force Measurement and Depth Profiling. *IEEE/ASME Trans. Mechatron.* **2025**, 1–9. DOI: 10.1109/TMECH.2025.3593334.

[48] Cho, G.; Im, J.; Kwon, H.; Song, C. An Optical Interferometer-Based Force Sensor System for Enhancing Precision in Epidural Injection Procedure. In 2024 IEEE/RSJ International Conference on Intelligent Robots and Systems (IROS), Abu Dhabi, United Arab Emirates, 2024, 8393–8399. DOI: 10.1109/IROS58592.2024.10802501.

[49] Zhang, T.; Chen, Y.; Ge, P.; Zou, Y. Lstm-Based External Torque Prediction for 6-Dof Robot Collision Detection. *J. Mech. Sci. Technol.* **2023**, *37*, 4847–4855. DOI: 10.1007/s12206-023-0837-3.

[50] Li, X.; Cao, L.; Tiong, A. M. H.; Phan, P. T.; Phee, S. J. Distal-End Force Prediction of Tendon-Sheath Mechanisms for Flexible Endoscopic Surgical Robots Using Deep Learning. *Mech. Mach. Theory* **2019**, *134*, 323–337. DOI: 10.1016/j.mechmachtheory.2018.12.035.

[51] Park, J.; Park, C. H. Recognition and Prediction of Surgical Actions Based on Online Robotic Tool Detection. *IEEE Robot. Autom. Lett.* **2021**, *6*, 2365–2372. DOI: 10.1109/LRA.2021.3060410.

[52] Lyu, C.; Guo, S.; Yan, Y.; Zhang, Y.; Zhang, Y.; Yang, P.; Liu, J. Deep Learning-Based Force Sensing Method for a Flexible Endovascular Surgery Robot. *IEEE Trans. Instrum. Meas.* **2024**, *73*, 1–10. DOI: 10.1109/TIM.2024.3381290.

[53] Wu, D.; Zhang, Y.; Ourak, M.; Niu, K.; Dankelman, J.; Vander Poorten, E. Hysteresis Modeling of Robotic Catheters Based on Long Short-Term Memory Network for Improved Environment Reconstruction. *IEEE Robot. Autom. Lett.* **2021**, *6*, 2106–2113. DOI: 10.1109/LRA.2021.3061069.

[54] Mihara, A.; Nishida, N.; Jiang, F.; Ohgi, J.; Imajo, Y.; Suzuki, H.; Funaba, M.; Yamagata, H.; Chen, X.; Sakai, T. Tensile Test of Human Lumbar Ligamentum Flavum: Age-Related Changes of Stiffness. *Appl. Sci.* **2021**, *11*, 3337. DOI: 10.3390/app11083337.

[55] Abbas, J.; Hamoud, K.; Masharawi, Y. M.; May, H.; Hay, O.; Medlej, B.; Peled, N.; Hershkovitz, I. Ligamentum Flavum Thickness in Normal and Stenotic Lumbar Spines. *Spine (Phila Pa 1976)* **2010**, *35*, 1225–1230. DOI: 10.1097/BRS.0b013e3181bfca15.